Built-in-Electric-Field Assisted Surface-Amorphized Nanocrystals for High-Rate Lithium-Ion Battery

Ting Xia,[1,] Wei Zhang,[2,*] James Murowchick,[3] Gao Liu,[2,**] Xiaobo Chen[1,**]*

[1]Department of Chemistry, University of Missouri – Kansas City, Kansas City, Missouri, 64110, USA; [2]Environmental Energy Technologies Division, Lawrence Berkeley National Laboratory, Berkeley, California 94720, USA; [3]Department of Geosciences, University of Missouri – Kansas City, Kansas City, Missouri 64110, USA.

KEYWORDS: Built-in electric field, surface amorphized nanocrystals, titanium dioxide, lithium ion battery.

ABSTRACT: High-power batteries require fast charge/discharge rates and high capacity besides safe operation. TiO_2 has been investigated as a safer alternative candidate to the current graphite or incoming silicon anodes due to higher redox potentials in effectively preventing the lithium deposition. However, its charge/discharge rates are reluctant to improve due to poor ion diffusion coefficients, and its capacity fades quickly with rate as only thinner surface layers can be effectively used in faster charge/discharge processes. Here, we demonstrated that surface-amorphized TiO_2 nanocrystals (SATNCs) greatly improve lithium ion rechargeable battery performances: 20 times rate and 340% capacity improvements, over crystalline TiO_2 nanocrystals (TNCs). This improvement is benefited from the built-in electric field (BIEF) within the nanocrystals. BIEF induces much lower lithium ion diffusion resistance and facilitates its transport in both insertion and extraction processes. This concept thus offers an innovative and general approach towards designing better-performance battery materials.

We are currently facing daily increased energy demand and decreased energy reserves. Tremendous effort has thus been devoted towards high-performance electrical/electrochemical energy-storage devices with both high power and high energy densities.[1-6] Widely studied as photocatalysts and dye-sensitized solar cell electrode,[7-11] titanium dioxide (TiO_2) has also been studied as an anode material for lithium ion batteries.[12-17] The diffusivity of Li in TiO_2 mostly depends on two major transport processes: the electronic conductivity and the Li^+ diffusivity.[18] However, only a thin surface layer of the host material is available for Li intercalation at high charging–discharging rates for bulk materials due to the low Li^+ ion diffusion coefficient (10^{-11} – 10^{-13} cm^2s^{-1})[15] and the low electronic conductivity (10^{-4} $S{\cdot}cm^{-1}$)[19] in the solid phase (Figure 1A). Decreasing the particle size into the nanometer-regime shortens the lithium diffusion length requirements, alters the electrochemical reactions and reactivity to Li and can increase the accessible volume to near-full capacity if the particle size is small enough (Figure 1B).[20-22] The size reduction, along with unique morphologies, leads to increased capacity beyond 0.5 Li per unit formula due to the surface-confined charge storage and different Li-reaction mechanisms from that in the bulk materials.[18] The reduction of the TiO_2 particle size, increase of high porosity and surface area are important to improve Li^+ diffusion due to the shorter Li^+ -diffusion length for filling the particles, interfacial (surface) Li storage.[18] However, so far, the rate performance of TiO_2 nanocrystalline electrode is still far from satisfactory.

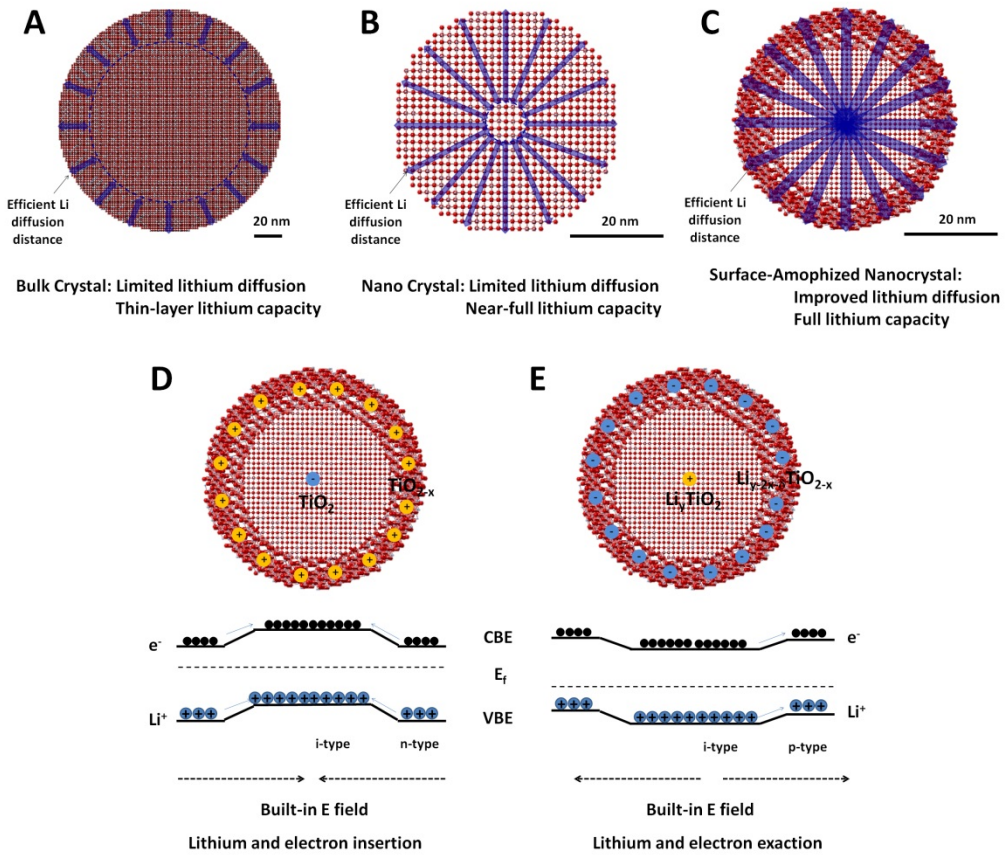

Figure 1. Comparison of charge diffusion in electrode materials made of (A) bulk crystals, (B) nanocrystals, (C) surface amorphized nanocrystals, and illustration of the facilitation of charge transport under the BIEF during discharge (D) and charge (E) processes. The length and the width of the arrows illustrate the relative penetration depth and the charge transfer/transport coefficients of the lithium ion in the material, respectively.

Here we develop two important contributions to help break this bottleneck. First, we create an amorphized non-stoichiometric outer layer on the nanocrystalline stoichiometric core to relieve the lattice distortion and to maintain the capacity retention during the Li^+ ion insertion/extraction process. In this layer, the overlap of the titanium and oxygen orbitals decreases, and the interaction between the transferred charge Li^+ and the host matrix becomes weaker. This will lead to an easier charge transport within the disordered layer (Figure 1C). Second, we create a built-in

electric field (BIEF) across the interface between the amorphized non-stoichiometric outer layer and the nanocrystalline stoichiometric core within the TiO_2 nanocrystals. This will facilitate the Li^+ ion in both insertion/extraction processes due to the BIEF. In order to realize this, we first create oxygen vacancy in the disordered layer. This will result TiO_{2-x}, a well-known n-type semiconductor.[8,23-25] Second, we keep the crystalline core with the stoichiometric formula of TiO_2, an typical i-type semiconductor.[23,25] Together, the TiO_{2-x}/TiO_2 shell/core will form an n-i heterojunction in the disordered/crystalline interface.[25] This will induce a BIEF across the interface. The direction of the BIEF will point to the core from the outer layer. Under this electric field, Li^+ diffusion will become much easier during the lithium discharge process, helping the Li^+ insertion (Figure D). Once Li^+ has been fully inserted or discharged into the nanocrystal, the core will become Li_yTiO_2, a presumably intrinsic semiconductor. The disordered layer will take much less Li^+ due to the existence of oxygen vacancy, and become $Li_{y-2x-\delta}TiO_{2-x}$, a relative p-type semiconductor to Li_yTiO_2. Again, this will form a new BIEF in the core/shell interface. The direction of the BIEF will point out to the disordered layer from the crystalline core. This will facilitate the Li^+ transport from the core to the shell, helping Li^+ extraction in the charge process (Figure 1E). Meanwhile, the movements of the electrons are less favored under the BIEF. As the electron diffusion coefficients are a few magnitudes higher than that of Li^+, it would only induce smaller increase of electron diffusion resistance, and gain a large reduction in the Li^+ diffusion resistance. Overall, the charge transport resistance will be largely lowered in this structure. If this proposed mechanism is proven to be valid, this mechanism and thus the current study will open a new concept for the lithium ion rechargeable battery research towards high-power applications.

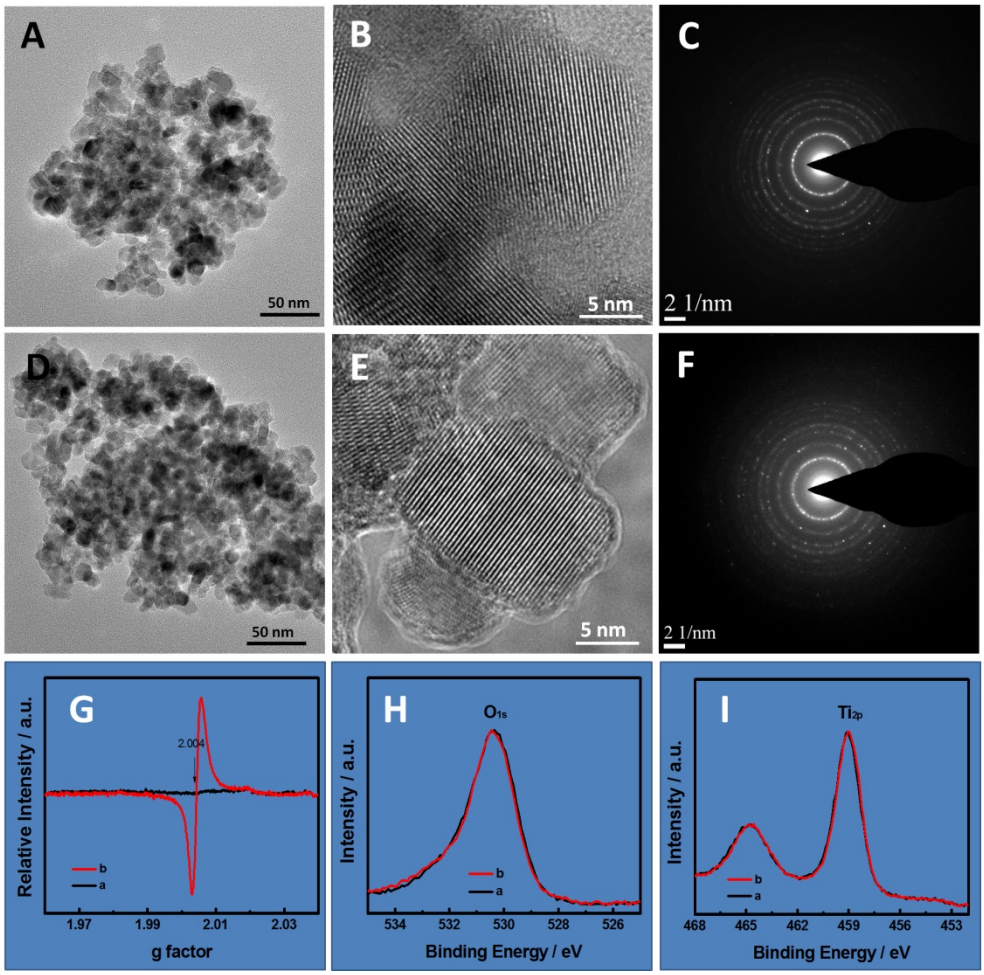

Figure 2. TEM, HRTEM images and SAED patterns of TNCs (A-C) and SATNCs (D-F), respectively. ESR (G), O1s (H) and Ti2p (I) core-level XPS spectra of TNCs (A-C) and SATNCs.

The BIEF assisted surface-amorphized titania nanocrystals (SATNCs) were obtained as follows. First, titinia nanocrystals (TNCs) were synthesized from a precursor solution consisting of titanium tetraisopropoxide, ethanol, hydrochloric acid, deionized water, and a polymer template, Pluronic F127. The solution was dried at 110 °C and the resulted powders were calcinated in air at 500 °C for 6 hours to remove the polymer template and to enhance their crystallization.[9,26] The BIEF assisted SATNCs nanoparticles were obtained through a high-

temperature vacuum process by placing the TNCs in a vacuum chamber at 500 ^{o}C for 4 hours. The key feature of this process was to create oxygen-vacancy adequate amorphous layer TiO_{2-x} on the surface, to effectively create the BIEF between the crystalline stoichiometric TiO_2 core and the oxygen-vacancy adequate amorphous layer TiO_{2-x} shell. To directly view the formation of the disordered layer on the surface, we performed transmission electron microscopy (TEM) studies on both samples (Figure 2). The TEM study was performed on a FEI Tecnai F20 TEM. The electron accelerating voltage was at 200 kV. Small amount of sample was first dispersed in water and then dropped onto TEM grids. The grids were then dried at 60 ºC overnight before TEM examination. The low resolution TEM images showed that the nanocrystals overlapped and aggregated over each other in both samples and their sizes were similar, in the range of 8 – 15 nm. The TNCs were highly crystalline throughout the whole particle as seen in the high-resolution TEM (HRTEM) image (Figure 2B), while SATNCs showed crystalline core with surface layered reconstructed with disorders forming an amorphous shell around 1~2 nm thickness (Figure 2E). The selected area electron diffraction pattern (SAED) (Figure 2C) showed clear anatase diffraction rings made of clean diffraction dots, suggesting the highly crystalline nature of the TNCs. A thick and milky diffraction background besides the anatase diffraction rings was apparently observed in the SAED of the SATNCs (Figure 2F), suggesting that the SATNCs probably also contained amorphous or disordered phases,[27,28] consistent with the HRTEM observation (Figure 2E).

Strong diffraction peaks in powder X-ray diffraction (PXRD) patterns suggested that both the TNCs and SATNCs had highly crystalline anatase phases (Figure S1A). The PXRD was performed on a Rigaku Miniflex PXRD machine with Cu Kα as the X-ray sources (wavelength = 1.5418 Å) and the 2-theta range was from 15º to 80º. The particle sizes estimated with the Scherrer equation[29,30] were similar, around 11 nm for both TNCs and SATNCs. We also studied the structural features of TNCs and SATNCs using Raman spectroscopy. The Raman spectra

were collected on an EZRaman-N benchtop Raman spectrometer. The Raman spectrometer was equipped with a 300 mW diode laser and the excitation wavelength was 785 nm. The spectrum range was from 100 cm^{-1} to 3100 cm^{-1}. The spectrum was averaged over three measurements to improve the signal-to-noise ratio. Raman spectra showed a very weak peak around 147.9 cm^{-1} (E_g) and a large luminescence background for the SATNCs, compared to strong highly crystalline anatase vibrational modes at 145.7 cm^{-1} (E_g), 199.1 cm^{-1} (E_g), 397.8 cm^{-1} (B_{1g}), 519.2 cm^{-1} (A_{1g} + B_{1g}), and 641.6 cm^{-1} (E_g) for the TNCs (Figure S1B).[9,29,30] This suggested an amorphous or disordered phase existed in SATNCs, likely on the outer layers, as the Raman is more sensitive to the surface structure than the XRD.[9,29,30]

To see if oxygen vacancy was successfully created in the SATNCs, we measured the electron spin spectra (ESR) of both samples. The ESR spectra were collected on a Benchtop Micro-ESR^{TM} machine, at a microwave frequency of 9.70 GHz at room temperature without light irradiation. The ESR data were calibrated in relation to g = 2.0066 of 2,2,6,6-tetramethyl-4-hydroxylpiperidine-1-oxyl. The scanning time was 30 s per sweep, and the spectrum was averaged after 30 sweeps. Quartz ESR tubes with an inner diameter of about 5.8 mm was used. The creation of oxygen vacancy was seen from the strong signal at g=2.004 (Figure 2G).[31] It is known that oxygen vacancies can be created by heating TiO_2 under ultra-high vacuum environment at high temperatures above normally 600°C.[23] The creation of oxygen vacancy in these TiO_2 nanocrystals at low vacuum levels and low temperature could be related to the reduced energies required to remove the oxygen from the lattice due to the nanoscale thermodynamic effect.[32,33] We also studied the surface chemical bonding and valence band information of the samples with X-ray photoelectron spectroscopy (XPS) on a PHI 5400 XPS system equipped with a conventional (non-monochromatic) Al anode X-ray source with K_α radiation. Small amount of TiO_2 nanocrystals were pressed onto conductive carbon tape for XPS measurements. The binding energies from the samples were calibrated, with respect to the C 1s

peak, from the carbon tape at 284.6 eV. The difference in the OH or Ti^{3+} contents of the TNCs and SATNCs could be generally ignored as seen from the almost identical O 1s and Ti 2p X-ray photoelectron spectra (XPS) (Figures 2H and 2I). In addition, the XPS surveys of both samples did not find other differences species as well (Figure S2). The location of the oxygen vacancy was more likely in the disordered outer layer, when considering the highly crystalline phases were almost identical and large structural alteration was observed in this layer. The formation of the amorphous phases could be attributed to the lattice relaxation or reorganization after the possible oxygen vacancy formation in the vacuum treatment under high temperature.[30]

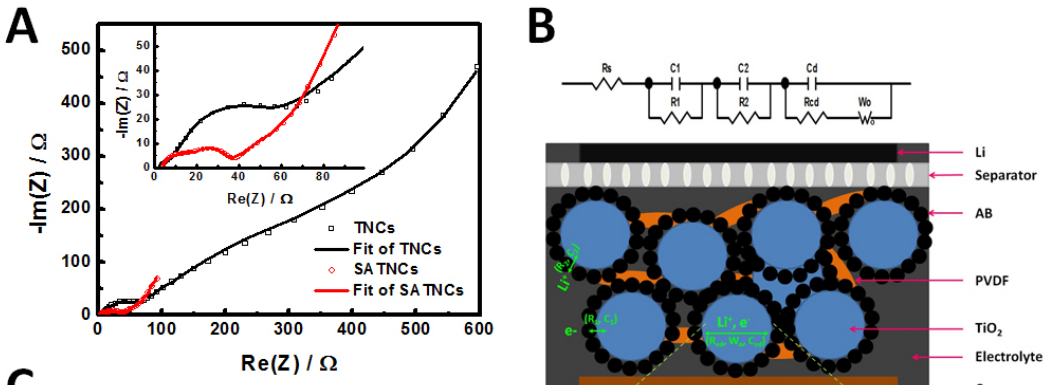

C

	Rs / Ω	R_1 / Ω	R_2 / Ω	R_{cd} / Ω
TNCs	3.1	28.9	34.9	2.2
SATNCs	4.3	6.9	12.67	8.0
	Wo-R / Ω	Wo-T / s	Wo-P	
TNCs	1287	67.3	0.39	
SATNCs	82.6	17.8	0.35	
		C_1 / F	C_2 / F	C_d / F
TNCs		4.2E-05	0.02	1.1E-06
SATNCs		9.5E-07	4.4E-05	5.4E-06

Figure 3. (A) EIS spectra of TNCs and SATNCs and their equivalent circuit fitting. (B) The equivalent circuit used to fit the EIS spectra and the corresponding components in the circuit and the battery. **Rs**: ohmic resistance, including the bulk resistance of the electrolyte, separator, and electrode; $\mathbf{R_1}$: electron transfer resistance at the carbon/TiO_2 electrode interface; $\mathbf{R_2}$: Li^+ transfer resistance in the TiO_2 electrode/electrolyte interface; $\mathbf{R_{cd}}$: interfacial charge transfer resistance of the interface between the surface layers and the bulk for TNCs, or the interface between the amorphized surface layers and the bulk for SATNCs; $\mathbf{W_o}$**-R**: Warburg charge diffusion resistance

in the TiO_2 electrode; **W_o-T**: Warburg diffusion time = L^2/D in the electrode, L is the length of the diffusion layer in the electrode, and D is the diffusion coefficient in the electrode; **W_o-P**: Warburg exponent; **C_1**: space charge capacitance in the carbon/TiO_2 electrode interface; **C_2**: double layer charge capacitance in the TiO_2 electrode/electrolyte interface; **C_d**: space charge capacitance of the interface between the surface layers (< 0.5 nm) and the bulk for TNCs, or the interface between the amorphized surface layers (1~2 nm) and the bulk for SATNCs. (C) The fitted EIS results from the equivalent circuits.

In order to confirm the facilitation of the charge transfer/transport across the crystalline matrix through a layer of oxygen vacancy–containing amorphized surface, electrochemical impedance spectra (EIS) were measured on both samples under the same condition (Figure 3A). The EIS measurements were perfomed on a Biologic potentiostat/EIS instrument. The frequency range was between 1 MHz and 10 mHz. The voltage modulation applied was 100 mV. All cells were cycled for two cycles and fully discharged to 1 V before EIS measurements. The equivalent circuit modeling[34] (Figure 3B) and fitting results (Figure 3C) suggested that the charge transfer and transport resistance was largely reduced for SATNCs compared over TNCs. The decrease/increase of charge transfer resistance at the interface for each component was accompanied with the decrease/increase of the capacitance for that component (i.e. $R_1 \sim C_1$, $R_2 \sim C_2$, and $R_{sd} \sim C_d$). The electron transfer resistance at the carbon/TiO_2 electrode interface (R_1) were reduced in the amophized surface from 28.9 to 6.9 and from 34.9 to 12.7 Ω, accompanied with its space charge capacitance decrease from 4.2×10^{-5} F to 9.5×10^{-7} F. The Li^+ transfer resistance in the TiO_2 electrode/electrolyte interface (R_2) was reduced in the amophized surface from 34.9 to 12.7 Ω, accompanied with its space charge capacitance decrease from 2.0×10^{-3} F to 4.4×10^{-5} F. The interfacial charge transfer resistance (R_d) between the amorphized surface layers and the bulk for the SATNCs (8.0 Ω) was slightly higher than that for the TNCs (2.2 Ω), accompanied

with its space charge capacitance increase to 5.4×10^{-6} F from 1.1×10^{-6} F. This indicated that lower charge capacitance or accumulation (C_1, C_2 and C_d) at the interface led to lower charge transfer resistance (R_1, R_2 and R_d), or the breakdown of the formation of charge accumulation in these interfaces could reduce charge transfer resistance, possibly due to the better adsorption and penetration into the amorphous layer. The higher space charge capacitance (C_d) at the amorphized/crystalline interface hinted the accumulation of the charge and the formation of the n-i heterojunction and the BIEF as illustrated in Figure 1D. The charge transport/diffusion resistance (W_o-R) in the SATNC electrode was much smaller (82.6 Ω) than that in TNC electrode (1287 Ω), further verifying the existence and the benefit of the BIEF on the charge transport. As the charge transport process was limited mainly by the most reluctant bulk diffusion in the electrode, the much smaller resistance (W_o-R) in the SATNC electrode induced much better rate performance. Overall, the charge accumulation layer at the interfaces was breakdown for charge transfer due to breakdown of the charge accumulation, and the charge transport resistance in the bulk was large reduced due to the driving force of the BIEF from the amorphized/crystalline interface, so the lithium ion battery performance was expected to be largely improved.

To validate our proposed approach, we tested the performance of made of SATNC and TNC electrodes in the half-cell configuration.[35,36] The preparation of the TiO_2 electrodes was conducted in an argon-filled glove box. The electrode mixture (82 wt% TiO_2, 8 wt% acetylene black and 10 wt% polyvinylidene fluoride) was steadily dispersed in N-methylpyrrolidone using a Polytron PT10-35 homogenizer at 2700 rpm for 30 minutes. The slurry was cast on a battery-grade copper sheet using a doctor blade. After being dried overnight, the electrodes were punched to 1/2" discs and dried in *vacuo* at 110°C overnight before being assembled into coin cells. The electrode loading was controlled at around 1.2 mg TiO_2/cm^2. Coin cell assembly was prepared in standard 2325 hardware under dry argon atmosphere. The separator was from Celgard (product 2400). 1M lithium hexafluorophosphate ($LiPF_6$) in ethylene carbonate (EC): diethyl carbonate (DEC) (1:2

weight ratio) was used as the electrolyte solution, and lithium as the counter electrode. Cells were discharged to 1.0 V and charged to 3.0 V after 15 min resting for the first cycle at C/25 (calculated from a specific capacity value of 335mAh/g) using a Maccor battery cycler at 30°C. For the 2nd cycle, cells were discharged to 1.0 V and charge to 3.0 V at C/5. Then the cells were cycled at 1C from 1.0 V to 3.0 V. One data point was recorded every 10 mV of voltage change. The initial discharge capacity of the SATNCs was 270 mAh/g at C/25 rate, 14% higher than that of the pristine TNCs (237 mAh/g) (Figures 4A). The discharge capacity of the SATNCs was 206 mAh/g at C/5 rate and 173 mAh/g at 1C rate for the second and third cycles, 27.2% and 25.4% higher than that of the TNCs (162 mAh/g and 138 mAh/g), respectively. After 500 charge/discharge cycles, the discharge capacity of the SATNCs was 131 mAh/g at 1C rate, 40.9% higher than that of the TNCs (93 mAh/g). For the first 50 charge/discharge cycles, the discharge capacity of the TNCs rapidly decreased and then increased quickly and then decreased slowly in the following cycles, while the discharge capacity of the SATNCs decreased very slightly (Figure 4B). Overall, the SATNCs showed around 40% improved discharge capacity over the crystalline TNCs.

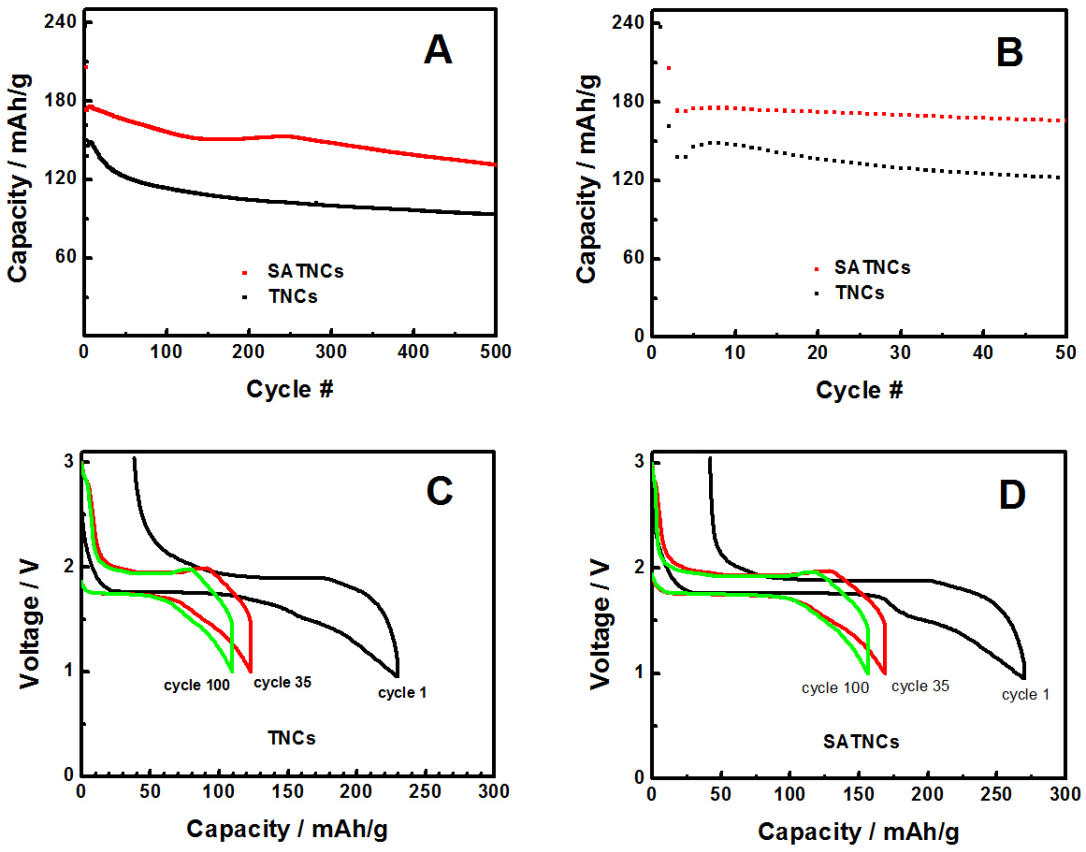

Figure 4. Variation of discharge capacity versus cycle number for TNCs and SATNCs for the first 500 cycles (A) and 50 cycles (B). The first cycle was conducted at C/25 rate, and the second cycle was conducted at C/5 rate, and the remaining cycles were conducted at 1C rate. Galvanostatic charge/discharge profiles with first cycle at C/25 rate, 35th cycle at 1C rate, and 100th cycle at 1C rate for the electrode made of TNCs (C) and SATNCs (D). The half cells were discharged to 1.0 V and charged to 3.0 V after 15 min resting for the first cycle at C/25 (calculated from a theoretical specific capacity value of 335 mAh/g). For the 2nd cycle, the cells were discharged to 1.0 V and charged to 3.0 V at C/5. Then the cells were cycled at 1C from 1.0 V to 3.0 V for over 500 cycles. Data were recorded for every 10 mV of voltage change.

Besides the larger charge/discharge capacity at various cycles, the SATNCs showed larger charge/discharge plateaus and smaller potential difference between the charge and discharge cycle. For example, the potential difference between the first charge and discharge cycle of the

SATNCs was about 0.11 V, 42.1% smaller than that of the TNCs (about 0.19 V) (Figures 4C and 4D). This smaller potential difference indicated the decreased charge transfer resistance and the larger charge/discharge plateaus suggest that the smoother charge transport and larger charge transport depth in the SATNCs.

Better discharge efficiency was also observed for the SATNCs over the TNCs in the 500 cycles test. The TNCs showed a quick drop of the discharge efficiency in the initial stage followed by a climb-up to the efficiency of around 99.6% after the first 50 cycles which was steady afterward for the remaining 450 cycles (Figure S3). The SATNCs showed a rapid climb in the initial few cycles to the efficiency of around 99.9% which was steady afterward for the remaining 500 cycles. A closer look at the first 20 cycles revealed that the discharge efficiency of the SATNCs increased steadily to the maximum within the first 4 cycles and followed with steady maximum efficiency in the next 16 cycles, while the discharge efficiency increased with large fluctuation for the TNCs in the first four cycles followed by slight decrease in the next 16 cycles. This smaller fluctuation could be due to a better structural accommodation of the lithium ions during the charge/discharge process in the reconstructed surface disordered layer in the SATNCs.

The SATNCs showed much better rate performance over the TNCs. The capacity of SATNCs was 175 mAh/g at 1C, 164 mAh/g at 10C, and 120 mAh/g at 50C, 11%, 56% and 243% higher than that of TNCs at the same conditions (Figures 5A). At the higher rate, 50C, the improvement was more apparent for the SATNCs over the TNCs. To reach certain capacity level, the SATNCs sustained much higher rate than crystalline TNCs. It took less than 3 min (> 20C) to charge the SATNCs to 156 mAh/g capacity, but it took around 1 hour to charge NTCs (Figures 5A and Table S1). Thus, the charging rate of the SATNCs was 20 times that of TNCs. The higher rate performance was possibly due to the lower lithium ion transport resistance as revealed by the EIS results in the charging and discharging processes in the SATNCs. This was in agreement with previous findings on the higher lithium ion capacities and capacity retention of amorphous over TNCs nanotubes.[37]

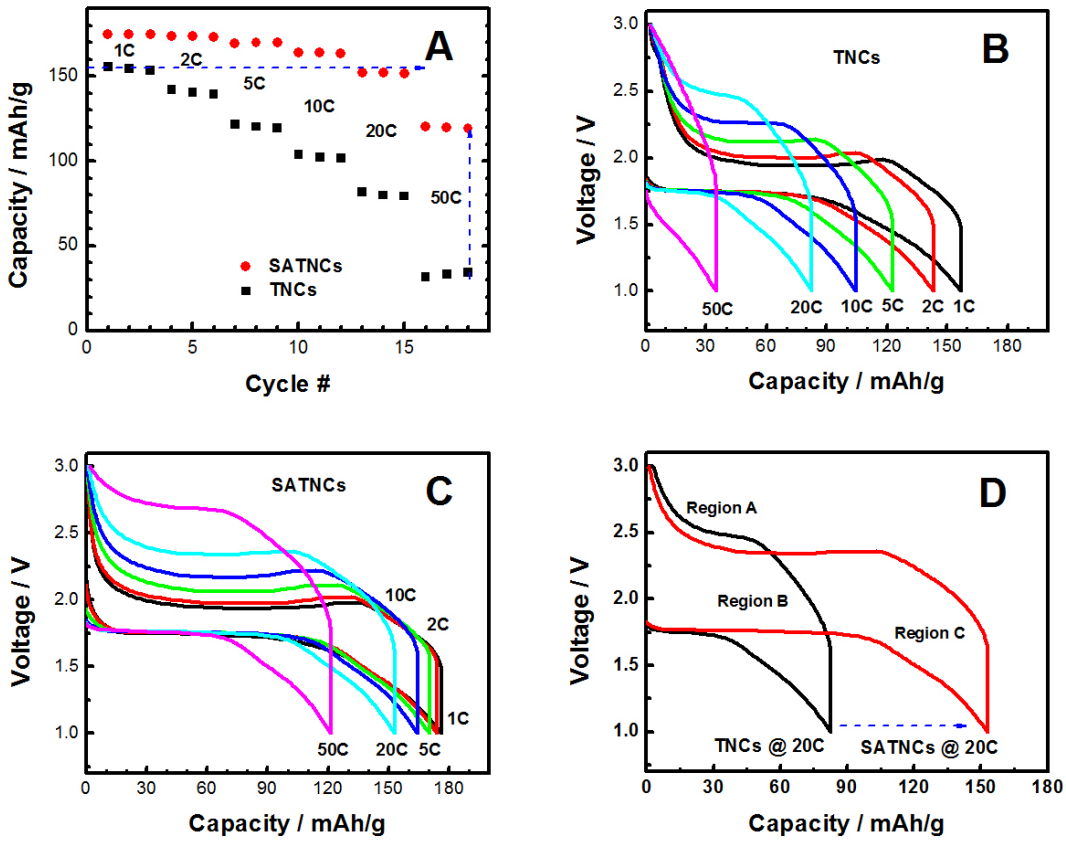

Figure 5. (A) Rate performances of the TNCs and the SATNCs. The charge rate was changed from 1C to 50C while the discharge rate was kept at 1C.The dashed horizontal line shows the rate improvement at the same capacity, and the dashed vertical line shows the capacity improvement at the same rate. Galvanostatic charge/discharge profiles at various charge rates for the electrode made of the TNCs (B) and SATNCs (C). (D) Comparison of the galvanostatic charge/discharge profiles for TNCs and the SATNCs at charge rates of 20C.

We further compared their galvanostatic charge/discharge profiles at various charging rates (Figures 5B and 5C). The SATNCs showed higher capacity and larger charge/discharge plateaus over the TNCs at each charging rate. The larger charge/discharge plateaus indicated that the smoother charge transport in the disordered layer was due to the weaker chemical bonding between the host matrix and the transferred charges. We also tested the rate performance of the

TNCs and the SATNCs when the charge/discharge rates were varied at the same time. The SATNCs outperformed the TNCs (Figure S4 and Table S2). For example, the capacity of SATNCs at 50C was 370% higher than that of TNCs at the same conditions. To reach 150 mAh/g capacity, it took around 1 hour (1C) to charge with crystalline TiO_2, but less than 30 min (> 2C) for SATNCs.

To understand why SATNCs had better performance than TNCs, we compared their galvanostatic charge/discharge profiles at rate 20C (Figure 5D). The discharge curve for the nanoporous anatase electrode was divided into three different voltage regions: [38-40] region A (> 1.75 V) - homogeneous Li insertion into the bulk, up to a solid-solution limit of Li in TiO_2, region B (≈ 1.75 V) - a typical biphase plateau with Li-rich phases coexisting with the Li-poor TiO_2 phase, and region C (< 1.75 V) -further reversible storage of Li at particle interfaces.[18] At voltages over 1.75 V, the phases no longer reversibly dissolved Li, although more Li was accommodated by further two-phase bulk intercalation ($x > 0.5$). The large increase of region B SATNCs was attributed to better bulk intercalation efficiency from the larger lithium diffusion coefficient and the increased electronic conductivity under the driving force of BIEF, and the shorter diffusion length of the crystalline phase in the SATNCs.

As additional notes, the BIEF mechanism proposed also successfully explains the large enhancement of the battery performance of previously reported crystalline-amorphous core-shell high-capacity and high-current silicon nanowire battery electrodes[3] and the recent high-rate oxygen-deficient $TiO_{2-\delta}$ nanoparticles[19] as well.

In summary, we have demonstrated that SATNCs as electrode materials for lithium ion batteries exhibited greatly improved lithium insertion/extraction performance compared with TNCs. This improvement is benefited from reduced charge diffusion resistance due to the BIEF. The concept of creating BIEF within the nanocrystal electrode materials via reconstructing the surface of crystalline electrode materials into amorphous structure at the nanometer scale is shown as a new approach for improving the battery performance. Although we did not measure the actual values of the BIEF within the nanocrystals, but from classical semiconductor theories,

we know that BIEF exists between the stoichiometric crystalline core and the amorphous shell with oxygen vacancy. The magnitude of the BIEF is expected depend on the oxygen vacancy content in the amorphous layer. The lithium ion transport is expected to depend on the thickness of the amorphous layer and the crystalline core. Thus, optimization of these parameters would probably further improve the performance of the electrode material. We are planning future experiments in revealing such relationship and measuring the actual values of the BIEF within each crystalline/amorphous nanocrystal. The amorphized layer coupled with the oxygen vacancy is necessary to make the BIEF with the crystalline core of stoichiometric composition. Meanwhile, we believe this concept can also be applied to other battery material systems such as $Li_4Ti_5O_{12}$, $LiMnO_2$ and $LiNiO_2$ to help realize the high-energy high-power electrical energy storage technologies. Creating BIEF within the nanocrystal electrode materials via other routes would also be feasible in other battery material systems such as Sn or Si.

Supporting Information. Experimental details, XRD, Raman, XPS survey, C 1s core-level XPS, Coulombic efficiency, and rate performances. This material is available free of charge via the Internet at http://pubs.acs.org.

Corresponding Author

* G. L. (GLiu@lbl.gov) and X. C. (chenxiaobo@umkc.edu).

Author Contributions

X.C. conceived the idea. T. X. performed the sample preparation, Raman and XRD measurements, W. Z. and G. L. performed the battery fabrication and testing. J. M. helped XRD measurements. X. C. conducted the TEM measurements. X. C. and G. L. co-wrote the paper. The manuscript was written through contributions of all authors. All authors have given approval to the final version of the manuscript. *These authors contributed equally.

ACKNOWLEDGMENT

X. C. thanks the support from College of Arts and Sciences, University of Missouri - Kansas City, the University of Missouri Research Board, and the generous gift from Dow Kokam. G. L. thanks the fund by the Assistant Secretary for Energy Efficiency, Office of Vehicle Technologies of the United States Department of Energy under Contract No. DE-AC03-76SF00098.

REFERENCES

1. Armand, M.; Tarascon, J. M. Building better batteries. *Nature* **2008**, *451*, 652 – 657.
2. Chan, C. K.; Peng, H.; Liu, G.; McIlwrath, K.; Zhang, X. F.; Huggins, R. A.; Cui, Y. High performance lithium battery anodes using silicon nanowires. *Nature Nanotech.* **2008**, *3*, 31-35.
3. Cui, L.-F.; Ruffo, R.; Chan, C. K.; Peng, H.; Cui, Y. Crystalline-amorphous core-shell silicon nanowires for high capacity and high current battery electrodes. *Nano Lett.* **2009**, *9*, 491-495.
4. Chan, C. K.; Zhang, X. F.; Cui, Y. High capacity Li-ion battery anodes using Ge nanowires, *Nano Lett.* **2008**, *8*, 307-309.
5. Chen, X.; Li, C.; Grätzel, M.; Kostecki, R.; Mao, S. S. Nanomaterials for renewable energy production and storage. *Chem. Soc. Rev.* **2012**, *41*, 7909 – 7937.
6. Shen, L.; Zhang, X.; Uchaker, E.; Yuan, C.; Cao, G. $Li_4Ti_5O_{12}$ nanoparticles embedded in a mesoporous carbon matrix as a superior anode material for high rate lithium ion batteries. *Adv. Energy Mater*. **2012**, *2*, 691 – 698.
7. Fujishima, A.; Honda, K. Electrochemical photolysis of water at a semiconductor electrode. *Nature* **1972**, *238*, 37 – 38.

8. Hagfeldtt, A.; Grätzel, M. Light-induced redox reactions in nanocrystalline systems. *Chem. Rev.* **1995**, *95*, 49 – 68.
9. Chen, X.; Liu, L.; Yu, P. Y.; Mao, S. S. Increasing solar absorption for photocatalysis with black hydrogenated titanium dioxide nanocrystals. *Science* **2011**, *331*, 746 – 750.
10. Wu, X.; Chen, Z.; Lu, G. Q.; Wang, L. Solar cells: nanosized anatase TiO_2 single crystals with tunable exposed (001) facets for enhanced energy conversion efficiency of dye-sensitized solar cells. *Adv. Funct. Mater.* **2011**, *21*, 4167 – 4172.
11. Chen, X.; Burda, C. The electronic origin of the visible-light absorption properties of C-, N- and S-doped TiO_2 nanomaterials. *J. Am. Chem. Soc.* 2008, *130*, 5018 – 5019.
12. Brutti, S.; Gentili, V.; Menard, H.; Scrosati, B.; Bruce, P. G. TiO_2-(B) nanotubes as anodes for lithium batteries: Origin and mitigation of irreversible capacity. *Adv. Energy Mater*. **2012**, *2*, 322 – 327.
13. Yang, Z.; Choi, D.; Kerisit, S.; Rosso, K. M.; Wang, D.; Zhang, J.; Graff, G.; Liu, J. Nanostructures and lithium electrochemical reactivity of lithium titanites and titanium oxides: A review. *J. Power Sources* **2009**, *192*, 588 – 598.
14. Wagemaker, M.; Kentgens, A. P. M.; Mulder, F. M. Equilibrium lithium transport between nanocrystalline phases in intercalated TiO_2 anatase. *Nature* **2002**, *418*, 397 – 399.
15. Moriguchi, I.; Hidaka, R.; Yamada, H.; Kudo, T.; Murakami, H.; Nakashima, N. A mesoporous nanocomposite of TiO_2 and carbon nanotubes as a high-rate Li-intercalation electrode material. *Adv. Mater.* **2006**, *18*, 69 – 73.

16. Li, N.; Liu, G.; Zhen, C.; Li, F.; Zhang, L.; Cheng, H.-M. Battery performance and photocatalytic activity of mesoporous anatase TiO_2 nanospheres/graphene composites by template-free self-assembly. *Adv. Funct. Mater.* **2011**, *21*, 1717 – 1722.
17. Lindström, H.; Södergren, S.; Solbrand, A.; Rensmo, H.; Hjelm, J.; Hagfeldt, A.; Lindquist, S.-E. Li^+ ion insertion in TiO_2 (anatase). 2. Voltammetry on nanoporous films. *J. Phys. Chem. B* **1997**, *101*, 7717 – 7722.
18. Shin, J.-Y.; Samuelis, D.; Maier, J. Sustained lithium-storage performance of hierarchical, nanoporous anatase TiO_2 at high rates: emphasis on interfacial storage phenomena. *Adv. Funct. Mater.* **2011**, *21*, 3464 – 3472.
19. Shin, J.-Y.; Joo, J. H.; Samuelis, D.; Maier, J. Oxygen-deficient $TiO_{2-\delta}$ nanoparticles via hydrogen reduction for high rate capability lithium batteries. *Chem. Mater.* **2012**, *24*, 543−551.
20. Wagemaker, M.; Borghols, W. J. H.; Mulder, F. M. Large impact of particle size on insertion reactions. A case for anatase Li_xTiO_2. *J. Am. Chem. Soc.* **2007**, *129*, 4323 – 4327.
21. Kavan, L.; Kalbac, M.; Zukalova, M.; Exnar, I.; Lorenzen, V.; Nesper, R.; Graetzel, M. Lithium storage in nanostructured TiO_2 made by hydrothermal growth. *Chem. Mater.* **2004**, *16*, 477 – 485.
22. Kim, J.; Cho, J. Rate characteristics of anatase TiO_2 nanotubes and nanorods for lithium battery anode materials at room temperature. *J. Electrochem. Soc.* **2007**, *154*, A542 – A546.
23. Diebold, U. The surface science of titanium dioxide. *Surf. Sci. Rep.* **2003**, *48*, 53 - 229.

24. Janotti, A.; Varley, J. B.; Rinke, P.; Umezawa, N.; Kresse, G.; van de Walle, C. G. Hybrid functional studies of the oxygen vacancy in TiO_2. *Phys. Rev.* **2010**, *81*, 085212.

25. Yu, P. Y.; Cardona, M. *Fundamentals of Semiconductors: Physics and Materials Properties*, Springer, Berlin, **2001**.

26. Chen, X.; Liu, L.; Liu, Z.; Marcus, M. A.; Wang, W.-C.; Oyler, N. A.; Grass, M. E.; Mao, B.; Glans, P.-A.; Yu, P. Y.; Guo, J.; Mao, S. S. Properties of disorder-engineered black titanium dioxide nanoparticles through hydrogenation. *Sci. Rep.* **2013**, *3*, 1510.

27. Champness, P. E. *Electron Diffraction in the Transmission Electron Microscope*, Taylor & Francis, **2001**.

28. Fultz, B.; Howe, J. *Transmission Electron Microscopy and Diffractometry of Materials*, Springer, New York, **2009**.

29. Xia, T.; Chen, X. Revealing the structural properties of hydrogenated black TiO_2 nanocrystals. *J. Mater. Chem. A* **2013**, *1*, 2983 – 2989.

30. Xia, T.; Zhang, W.; Murowchick, J.; Liu, G.; Chen, X. A facile method to improve the photocatalytic and lithium-ion rechargeable battery performance of TiO_2 nanocrystals. *Adv. Energy Mater.* **2013**, DOI: 10.1002/aenm.201300294.

31. Nakamura, I.; Negishi, N.; Kutsuna, S.; Ihara, T.; Sugihara, S.; Takeuchi, K. Role of oxygen vacancy in the plasma-treated TiO_2 photocatalyst with visible light activity for NO removal. *J. Molecul. Catal. A* **2000**, *161*, 205 - 212.

32. V. Berube, G. Radtke, M. Dresselhaus, G. Chen, Size effects on the hydrogen storage properties of nanostructured metal hydrides: A review. *Int. J. Energy Res.* **2007**, *31*, 637-663.

33. A. P. Alivisatos, Perspectives on the physical chemistry of semiconductor nanocrystals. *J. Phys. Chem.* **1996**, *100*, 13226 -13239.

34. Orazem, M. E. & Tribollet B. *Electrochemical impedance spectroscopy*. John Wiley & Sons, Oct 13, 2011, NJ, USA.

35. Liu, G.; Xun, S.; Vukmirovic, N.; Song, X.; Olalde-Velasco, P.; Zheng, H.; Battaglia, V. S.; Wang, L.; Yang, W. Polymers with tailored electronic structure for high capacity lithium battery electrodes. *Adv. Mater.* **2011**, *23*, 4679 – 4683.

36. Xia, T.; Zhang, W.; Li, W.; Oyler, N. A.; Liu, G.; Chen, X. Hydrogenated surface disorder enhances lithium ion battery performance. *Nano Energy* **2013**, DOI: /10.1016/j.nanoen.2013.02.005.

37. Guan, D.; Cai, C.; Wang, Y. Amorphous and crystalline TiO_2 nanotube arrays for enhanced Li-ion intercalation properties. *J. Nanosci. Nanotechnol.* **2011**, *11*, 3641 – 3650.

38. Guo, Y.-G.; Hu, Y.-S.; Sigle, W.; Maier, J. Superior electrode performance of nanostructured mesoporous TiO_2 (anatase) through efficient hierarchical mixed conducting networks. *Adv. Mater.* **2007**, *19*, 2087 – 2091.

39. Guo, Y.-G.; Hu, Y.-S.; Maier, J. Synthesis of hierarchically mesoporous anatase spheres and their application in lithium batteries. *Chem. Commun.* **2006**, 2783 – 2785.

40. Guo, Y.-G.; Hu, Y.-S.; Sigle, W.; Maier, J. Superior electrode performance of nanostructured mesoporous TiO_2 (anatase) through efficient hierarchical mixed conducting networks. *Adv. Mater.* **2007**, *19*, 2087 – 2091.

SYNOPSIS

Surface-amorphized TiO_2 nanocrystals (SATNCs) benefited from the built-in electric field (BIEF) within the nanocrystals greatly improve lithium ion rechargeable battery performances: 20 times rate and 340% capacity improvements, over crystalline TiO_2 nanocrystals (TNCs), due to the reduced lithium ion diffusion resistance in both charge and discharge processes.